

# Surface Plasmon Resonances of Silver Triangle Nanoplates: Graphic Assignments of Resonance Modes and Linear Fittings of Resonance Peaks

Yi He and Gaoquan Shi\*

Department of Chemistry and Bio-organic Phosphorous Lab, Tsinghua University, Beijing 100084, People's Republic of China

Received: May 18, 2005; In Final Form: July 21, 2005

The extinction spectra of five silver equilateral triangle plates with a fixed thickness of 10 nm and side lengths of 50, 100, 150, 200, and 250 nm, respectively, have been simulated by the discrete dipole approximation (DDA) method in which a geometric object of interest is meshed and represented by a lattice of spatial dipoles. Irradiated by an incident plane wave with a given propagation direction and polarization state, each triangle nanoplate presents three surface plasmon resonance (SPR) peaks in the range of 300 to 1200 nm. At a given peak, every complex spatial oscillatory vector derived by DDA (corresponding to a certain dipole in the meshed target) is orthogonally resolved into three basic oscillations. Each basic component can be subsequently expressed by two parameters, amplitude ( $P$ ) and phase angle ( $\varphi$ ). The distributions of six such physical parameters of all the dipoles in the selected cross plane of the target are illustrated colorfully in plots as a graphic characterization and assignment of the SPR modes. The graphic method is applied to reveal the local fine features of SPR modes. And it provides direct evidence for classifying SPR peaks which belong to different triangle nanoplates and appear at different wavelengths. Three SPR modes are recognized graphically and the wavelengths of SPR peaks are found to have linear relationships with the side lengths of the triangle nanoplates.

## 1. Introduction

The fabrication of metal nanoparticles has attracted steadily growing attention due to their fascinating optical and electrical properties, which are different from those of corresponding single atom or bulk solid.<sup>1</sup> Nanoparticles with various shapes such as spheres,<sup>2</sup> cubes,<sup>3</sup> stars,<sup>4</sup> rods,<sup>5</sup> and wires<sup>6</sup> have been synthesized and characterized. Among those the nanoplates of noble metals are noticeable for their 2-D structures.<sup>7</sup> Recently, colloid chemistry has obtained great development in the synthesis of well-defined silver trigonal nanoplates, whose extinction spectra are quite different from those of spherical nanoparticles and present surface plasmon resonance (SPR) peaks at relatively long wavelengths.<sup>8</sup> The color of these triangle nanoplates is unusually red due to distinct scattering in this wavelength range. As we know, the SPR absorption and scattering of the metal nanoparticles are caused by the oscillation of the collective conductive electrons of the particles and remarkably depend on particle shapes.<sup>9</sup> In addition, the particle size is also an important factor to the SPR wavelength, and many papers concerning the size effect of the spherical nanoparticles have been published.<sup>10</sup> Naturally, geometrical parameters also have strong influences on the SPR peaks of triangle nanoplates. Schatz and co-workers have demonstrated that the increase of the side length of triangle nanoplates could lead their SPR peak to red shift by several hundred nanometers.<sup>11</sup> This controllable optical property in terms of wavelength is quite exciting and interesting, and it enables the particles to be applied in biological sensing and drug delivery.<sup>12</sup> Because the photons with near-IR wavelengths can harmlessly pass through biological tissues, nanoplates with high extinction coefficients at the target tissues will convert the near-IR photons to heat at high yields. So they

can be used in photothermal cancer therapy and photothermally triggered drug release. For a better control of the SPR wavelengths, a clear relationship between the geometrical factors and SPR wavelengths should be established quantitatively. It requires a more clear understanding and a more detailed theoretical analysis about the interaction between metallic nanoparticles and electromagnetic incidences.

The study of the colors of metal nanoparticles can be traced back to 19th century when Michael Faraday studied the color of gold colloid in stained glass windows.<sup>13</sup> Mie presented an analytical solution to Maxwell's equations which describe a isolated spherical particle in 1908.<sup>14</sup> Over the last three decades several numerical methods based on finite elements have been developed for overcoming the limitation in calculations of particles with arbitrary shape and multicomposition.<sup>15</sup> Among those the discrete dipole approximation (DDA) has been proven to be an effective method for estimating the optical properties of metal particles in nanoscale.<sup>16</sup> In most cases the extinction spectra of metal nanoparticles under different conditions were simulated by the DDA method and compared with the experimental results.<sup>4b,7a,8a,17</sup> The investigation of the influence of particle shapes on surface SPR wavelengths was also performed by this method.<sup>18</sup> For a sphere, its simulated spectrum may have several SPR peaks attributed to the absorption and scattering of dipolar mode, quadrupolar mode, and higher order mode.<sup>19</sup> For a nonspherical target, through an empirically analogical extension from the situation of nanospheres, peaks in the spectra were usually assigned as dipole or multipole resonances. Such assignments can give only the outline features of SPR modes of the particles with nonspherical shapes, but cannot reveal their detailed information that can be regarded as fingerprints of the SPR modes. For instance, it is hard to image the dipolar modes of a tetrahedron or a triangle prism nanoparticle, which are

\* To whom correspondence should be addressed. Phone: 86-10-62773743. Fax: 86-10-62771149. E-mail: gshi@tsinghua.edu.cn.

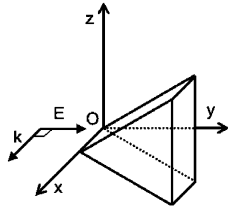


**Figure 1.** Geometric setup of the triangle nanoplate and the incident wave plane.

strongly related to the local light intensity, while these details are necessary for the investigation of near-field phenomenon. Furthermore, they are also useful for classifying SPR peaks. Yet up to now only a few papers concerned this detailed subject.<sup>20</sup> In fact, to characterize the nature of a SPR mode by the DDA method, all the dipoles used to represent the target of interest should be considered. Each dipole is a complex spatial vector and consists of three basic oscillatory components along *x*-, *y*- and *z*-axes, and each component has two parameters, amplitude and phase angle. Thus, six parameters should be taken into account just for a single dipole. Generally, the DDA method will mesh the target into *N* dipoles (*N* ranges from 10 000 to 1 000 000) and the dipoles have totally 6*N* parameters. What is more, these dipoles are distributed in the 3-dimensional space defined by the target (here is the triangle nanoplate as demonstrated in Figure 1) and cannot be imaged in a plane. Due to the complexity, we suggest an approach that selects some dipoles in the model and illustrate their parameters in six separate plots to represent and characterize a certain SPR mode. In this paper, the graphic method has been applied to investigate the SPRs of five triangle nanoplates with the same thickness and different side lengths. Three distinct SPR modes are recognized and assigned by this method. The wavelengths of each SPR mode are found to have linear relationships with the side length of the triangle nanoplate.

## 2. Methods and Models

**2.1. Discrete Dipole Approximation (DDA).** The DDA method requires the geometric object of interest to be represented by a cubic array of *N* point dipoles, *P*<sub>1</sub>, ..., *P*<sub>*N*</sub>. The *i*th oscillatory dipole **P**<sub>*i*</sub> with polarizability α<sub>*i*</sub> is induced by **E**(**r**<sub>*i*</sub>), the total electric field at **r**<sub>*i*</sub>.

$$\mathbf{P}_i \exp(-i\omega t) = \alpha_i \mathbf{E}(\mathbf{r}_i) \exp(-i\omega t) \quad (1)$$

Here ω is the frequency of the incident plane wave and **E**(**r**<sub>*i*</sub>) is the sum of the electric field of incident plane wave **E**<sub>inc</sub>(**r**<sub>*i*</sub>) and contributions of all other dipoles in the object **E**<sub>dipoles</sub>(**r**<sub>*i*</sub>).

$$\mathbf{E}(\mathbf{r}_i) = \mathbf{E}_{\text{inc}}(\mathbf{r}_i) + \mathbf{E}_{\text{dipoles}}(\mathbf{r}_i) = \mathbf{E}_0 \exp(i\mathbf{k} \cdot \mathbf{r}_i) - \sum_{j \neq i} \mathbf{A}_{ij} \mathbf{P}_j \quad (2)$$

In eq 2, **E**<sub>0</sub> and **k** are the amplitude and wave vector of the incident light, respectively, and -**A**<sub>*ij*</sub>**P**<sub>*j*</sub> is the induced electric field of the *j*th dipole at the position of the *i*th one and can be expressed by eq 3

$$\mathbf{A}_{ij} \mathbf{P}_j = \frac{\exp(ikr_{ij})}{r_{ij}^3} \left( k^2 \mathbf{r}_{ij} \times (\mathbf{r}_{ij} \times \mathbf{P}_j) + \frac{1 - ikr_{ij}}{r_{ij}^2} [r_{ij}^2 \mathbf{P}_j - 3\mathbf{r}_{ij}(\mathbf{r}_{ij} \cdot \mathbf{P}_j)] \right) \quad (3)$$

where **r**<sub>*ij*</sub> = **r**<sub>*i*</sub> - **r**<sub>*j*</sub> and *r*<sub>*ij*</sub> is the magnitude of the vector. Substitute (2) into (1) and omit the frequency factor exp(-iωt)

on both sides and we obtain an equation set (4) of *N* equations that represents *N* three-dimensional vectors.

$$\alpha_i^{-1} \mathbf{P}_i + \sum_{j \neq i} \mathbf{A}_{ij} \mathbf{P}_j = \mathbf{E}_0 \exp(i\mathbf{k} \cdot \mathbf{r}_i), \quad i = 1, \dots, N \quad (4)$$

The relation between polarizabilities of dipoles and dielectric constants of materials at a given wavelength can be established by using the lattice dispersion relation (LDR) derived by Draine and Goodman.<sup>21</sup>

$$\alpha_i = \frac{\alpha_i^{\text{LDR}}}{1 - (2/3)ik^3 \alpha_i^{\text{LDR}}} \quad (5)$$

$$\alpha_i^{\text{LDR}} = \frac{\alpha_i^{\text{CM}}}{1 + \alpha_i^{\text{CM}}(b_1 + b_2 \epsilon_i + b_3 S \epsilon_i)(k^2/d)} \quad (6)$$

$$\alpha_i^{\text{CM}} = \frac{3d^3(\epsilon_i - 1)}{4\pi(\epsilon_i + 2)} \quad (7)$$

Here *b*<sub>1</sub>, *b*<sub>2</sub>, *b*<sub>3</sub>, and *S* are the coefficients obtained by integrals, *d* is the lattice spacing of the dipole array, ε<sub>*i*</sub> is the complex dielectric constant of the material of the *i*th dipole, and α<sub>*i*</sub><sup>CM</sup> is the classical Clausius–Mossotti relation. This corrected Clausius–Mossotti relation has proven to achieve more accurate results than other prescriptions.<sup>21</sup> Note the dielectric constant of silver is a variable within the wavelength range investigated. The values at different wavelengths have been measured experimentally<sup>22</sup> and utilized in our calculations.

The DDSCAT program<sup>23</sup> developed by Draine and Goodman was compiled to solve the equation set (4). After an iterative calculation, this freely available software reaches the numerical results of the dipoles within the allowed error, and then evaluates the extinction, absorption, and scattering efficient factors *Q*<sub>ext</sub>, *Q*<sub>abs</sub>, and *Q*<sub>sca</sub>, following eqs 8,

$$Q_{\text{ext}} = C_{\text{ext}}/\pi a_{\text{eff}}^2, \quad Q_{\text{abs}} = C_{\text{abs}}/\pi a_{\text{eff}}^2, \quad Q_{\text{sca}} = Q_{\text{ext}} - Q_{\text{abs}} \quad (8)$$

where *a*<sub>eff</sub> is the effective radius of the particle and *C*<sub>ext</sub> and *C*<sub>abs</sub> are calculated by using the optical theorem (9) and (10),<sup>24</sup> where the superscript asterisk denotes the conjugate complex.

$$C_{\text{ext}} = \frac{4\pi k}{|\mathbf{E}_0|^2} \sum_{i=1}^N \text{Im}(\mathbf{E}_{\text{inc}}(\mathbf{r}_i) \cdot \mathbf{P}_i) \quad (9)$$

$$C_{\text{abs}} = \frac{4\pi k}{|\mathbf{E}_0|^2} \sum_{i=1}^N \left\{ \text{Im}[\mathbf{P}_i \cdot (\alpha_i^{-1})^* \mathbf{P}_i^*] - \frac{2}{3} k^3 \mathbf{P}_i \cdot \mathbf{P}_i^* \right\} \quad (10)$$

Since the program does not output the dipole data directly, a few program codes were inserted to transfer these data from the computer memory to a file that serves as an interface between the DDSCAT program and the homemade graphic analytical program. There is not any adaptation about the algorithm in original codes.

## 2.2. Meshing and Geometric Setup of Triangle Nanoplates.

In the DDA method, the meshing of the target is completely flexible. It only requires the interdipole spacing *d* to be small enough compared with any structural feature of the target and the wavelength λ. In this paper, five silver triangle nanoplates with fixed thickness of 10 nm and side lengths of 50, 100, 150, 200, and 250 nm are all meshed with a 1 nm cubic grid. These

nanoplates are supposed to be isolated in a vacuum (relative permittivity of the medium equals 1), so there is not a surrounding to be meshed. As the results of the meshing, these nanoplates are represented by 10 830, 43 290, 97 420, 173 190, and 270 630 dipoles and denoted by 50-10, 100-10, 150-10, 200-10, and 250-10, respectively. The meshing is fine enough since  $d = 1$  nm is much smaller than any structural sizes of these triangle nanoplates (10 nm at least). It also satisfies the limitation of the wavelength, which can be formularly expressed as  $|m|kd < 0.5$  (here  $m$  is the complex refractive index of silver and  $k = 2\pi/\lambda$  is the magnitude of wave vector  $\mathbf{k}$ ). In our calculations, the values of  $|m|kd$  at different wavelengths are always less than 0.05, only a tenth of the threshold value. Moreover, Schatz et al. have adopted lattice spacings of 1 and 2 nm to simulate the extinction spectra of silver snipped nanoprisms in aqueous medium and the results fit well with the experimental measurements.<sup>8a</sup>

One representative geometric setup was taken into account for the spectra calculations of the five triangle nanoplates. As Figure 1 shows, the triangle nanoplate of interest was set in a rectangular coordinate system with one vertex possessing the origin and one edge following the positive direction of the  $x$ -axis, and the whole target is symmetric about the  $xOy$  plane. The incident plane wave propagates along the  $x$ -axis, and its electric field polarizes along the  $y$ -axis. It should be mentioned that the propagation direction of the incident plane wave and its polarization state, especially the latter, may influence the simulated spectral curve notably. In this paper, we mainly focus on the introduction of a graphic assignment method and the dependence of the SPRs of triangle nanoplates on their side lengths. So the effect of the propagation direction and polarization state of the incidence on the spectra and SPR modes will be discussed elsewhere.

**2.3. Graphic Assignments of SPR Modes.** During the spectral simulation of a given silver triangle nanoplate, the equation set (4) were iteratively solved for every integer wavelength among 300 to 1200 nm, respectively. The solutions of (4),  $\mathbf{P}_1, \dots, \mathbf{P}_N$  were achieved and stored for each integer wavelength, including those at SPR peaks. Each vector in the solutions belongs to an individual dipole, for example,  $\mathbf{P}_i$  corresponds to the  $i$ th dipole and describes the oscillation of negative local conduction electrons relative to the quasistatic positive crystal lattice at the neighborhood of the point  $r_i$ . Thus, the ensemble of the solutions for a certain SPR peak will give an overall view of the oscillation of collective conductive electrons of the silver triangle nanoplate, which is a so-called surface plasmon resonance at this peak wavelength. It indicates that a complete analysis of the solutions at the SPR peak will reveal the character of the corresponding SPR mode, overall or in detail. However, there are some difficulties in imaging a SPR mode simply according to the original solutions for the SPR peak.

First,  $\mathbf{P}_i$  is not a simple value but a complex vector that needs to be resolved into three complex numbers  $C_{i,x}$ ,  $C_{i,y}$ , and  $C_{i,z}$  for further processing. These three complex numbers stand for three basic vibratory components along three main axes respectively and can be expressed in their exponential forms as eq 11.

$$\mathbf{P}_i = C_{i,x}\hat{\mathbf{x}} + C_{i,y}\hat{\mathbf{y}} + C_{i,z}\hat{\mathbf{z}} = P_{i,x}\exp(i\varphi_{i,x})\hat{\mathbf{x}} + P_{i,y}\exp(i\varphi_{i,y})\hat{\mathbf{y}} + P_{i,z}\exp(i\varphi_{i,z})\hat{\mathbf{z}} \quad (11)$$

Here  $P_{i,x}$ ,  $P_{i,y}$ , and  $P_{i,z}$  are amplitudes of the basic oscillations,  $\varphi_{i,x}$ ,  $\varphi_{i,y}$ , and  $\varphi_{i,z}$  are their phase angles. Remember that the

**TABLE 1: Sketches of Charge Distribution of Two Adjacent Oscillations with a Phase Difference of  $\varphi_2 - \varphi_1$  at Moment  $t^a$**

$t \backslash \varphi_2 - \varphi_1$	0	1/4 T	1/2 T	3/4 T	T
90°					
-90°					
0°					
180°					

<sup>a</sup> Here  $\times$  means a zero dipole.

frequency factor  $\exp(-i\omega t)$  in eq 1 has been omitted during the equation deriving process. So the integrated form of the  $\mathbf{P}_i$  should be  $\mathbf{P}_i \exp(-i\omega t)$ , which can be written as eq 12.

$$\mathbf{P}_i \exp(-i\omega t) = P_{i,x} \exp(i\varphi_{i,x} - i\omega t)\hat{\mathbf{x}} + P_{i,y} \exp(i\varphi_{i,y} - i\omega t)\hat{\mathbf{y}} + P_{i,z} \exp(i\varphi_{i,z} - i\omega t)\hat{\mathbf{z}} \quad (12)$$

As we all know, it takes three parameters to determine a basic oscillation: amplitude, frequency, and phase angle. In eq 12, the frequency  $\omega$  is determined by wavelength  $\lambda$  following  $\omega = 2\pi c/\lambda$  ( $c$  denotes the velocity of light in a vacuum) and it does not change from dipole to dipole at a given wavelength. Thus,  $\omega$  can be regarded as a constant and omitted in this study. As a result, there are only two parameters remaining for each basic oscillation and totally six parameters for each dipole. The distributions of amplitude always draw much attention due to its close relation to the nonlinear near-field optics.<sup>20</sup> Here, we desire to emphasize the influence of the distribution of phase angle. Considering two adjacent basic oscillations,  $P \exp(i\varphi_1 - i\omega t)\hat{\mathbf{y}}$  and  $P \exp(i\varphi_2 - i\omega t)\hat{\mathbf{y}}$ , they are along the same direction  $\hat{\mathbf{y}}$  and have the same amplitude  $P$ . Supposing  $\varphi_1 = 0^\circ$ , to phase difference of  $\varphi_2 - \varphi_1$ , the sketches of charge distribution at moment  $t$  are illustrated in Table 1 (where  $T = 2\pi/\omega$  is the period of the oscillations). It is clear from this table that various phase differences will result in completely different charge distributions. The first oscillation (shown as the left one in each pane of Table 1) will be ahead or lags behind the second one (the right one in each pane) according to the value of  $\varphi_2 - \varphi_1$ . In addition, the phase angle is also important to an individual complex oscillation, which can be resolved into several basic oscillations, for example,  $P \exp(i\varphi_x - i\omega t)\hat{\mathbf{x}} + P \exp(i\varphi_y - i\omega t)\hat{\mathbf{y}}$ . This complex oscillation has two basic oscillations along  $\hat{\mathbf{x}}$  and  $\hat{\mathbf{y}}$  directions, respectively. Supposing  $\varphi_x = 0^\circ$ , to the phase difference of  $\varphi_y - \varphi_x$ , the sketches of charge distributions at moment  $t$  are illustrated in Table 2. The resultant oscillation gives a circular or linear track. Generally, the track will be an ellipse and its ellipticity is determined by the value of  $\varphi_y - \varphi_x$ . Since both amplitude and phase angle of dipoles are crucial factors, we illustrate the six parameters in six pictures respectively and then combine the patterns into one as a graphic characterization of the SPR mode.

The second difficulty is that all the dipoles in the meshed target are not in a particular plane and we cannot map the ensemble into one figure. Therefore, some key planes were



**TABLE 2: Sketches of Charge Distributions of a Complex Oscillation with Phase Difference of  $\varphi_y - \varphi_x$  at Moment  $t^a$** 

$t$ $\varphi_y - \varphi_x$	0	1/4 T	1/2 T	3/4 T	T
90°					
-90°					
0°		×		×	
180°		×		×	

<sup>a</sup> Here × means a zero dipole

considered primarily and the dipoles in these planes were illustrated by six-parameter graphs to represent the features of the SPR mode. In this paper, all planes are denoted by corresponding plane equations in analytic geometry. For example, we use  $x = 0$  to indicate the  $yOz$  plane in Figure 1, and the dipoles of the triangle nanoplate 50-10 in this plane are shown in Figure 2. Each circle in the figure stands for a dipole and will be replaced by a certain color in the distribution plots of amplitudes or phase angles.

### 3. Results and Discussion

**3.1. The Extinction Spectra and SPR Peaks.** The calculated extinction spectra of the five triangle nanoplates are illustrated in Figure 3. In the range of 300 to 1200 nm, each spectrum presents three SPR peaks, and the most intensive peak always has the longest wavelength. Thus, these five dominant SPR

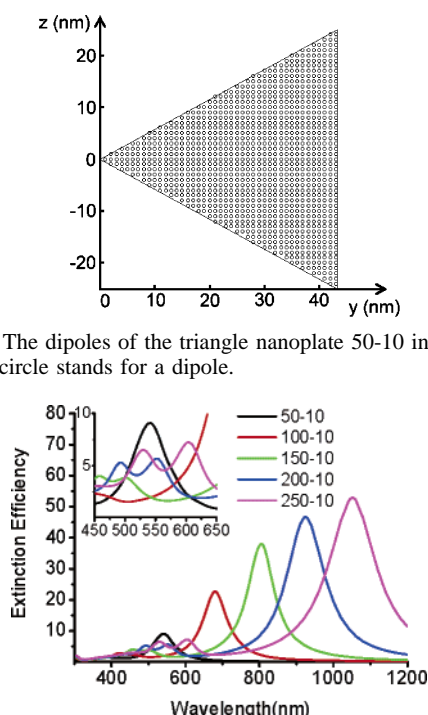


**Figure 2.** The dipoles of the triangle nanoplate 50-10 in the plane  $x = 0$ ; each circle stands for a dipole.

**Figure 3.** The calculated extinction spectra of the five triangle nanoplates 50-10, 100-10, 150-10, 200-10, and 250-10. The inset shows a magnification of the spectra in the range of 450 to 650 nm.

**TABLE 3: The Wavelengths (nm) of the SPR Peaks of the Five Triangle Nanoplates**

	50-10	100-10	150-10	200-10	250-10
Mode-I	541	680	805	924	1052
Mode-II	413	458	503	552	604
Mode-III	385	420	456	492	529

peaks are regarded as a mode and denoted by Mode-I. From right to left, the second and third peaks of a spectrum are denoted by Mode-II and Mode-III, respectively, and the wavelengths of these SPR modes are summarized in Table 3. In fact, according to the literature about the spherical silver particles, the three modes can be regarded as dipolar, quadrupolar, and octupolar resonances, respectively.<sup>19</sup> Because it is not clear whether the assignments of spherical silver nanoparticles can be extended to the systems of nonspherical nanoparticles, we will use our own denotations in this work. Note that the classification of the peaks based on their relative positions in the spectra is experiential and there is a lack of direct evidence. So a detailed analysis is necessary to reveal the characters of each SPR mode and establish the foundations of the classification. The facile graphic method described above will provide an effective approach for this purpose.

**3.2. The Selection of the Key Planes.** Since key planes are required in the six-parameter graphic method, here we take the triangle nanoplate 150-10 irradiated by an incidence with a wavelength of 805 nm as an example to demonstrate how to determine a key plane for characterizing the SPR mode. Figure 4 illustrates the dipoles in the plane  $x = 0$  by the six-parameter graphic method. The three plots on the left correspond to the distributions of three phase angles  $\varphi_x$ ,  $\varphi_y$ , and  $\varphi_z$ . As we know, the phase angle has a period of 360°, so its value is restricted between  $-180^\circ$  and  $+180^\circ$ . A periodical color bar is attached to the left of each plot and the value of the phase angle of each dipole can be roughly estimated from this bar. Note that if we

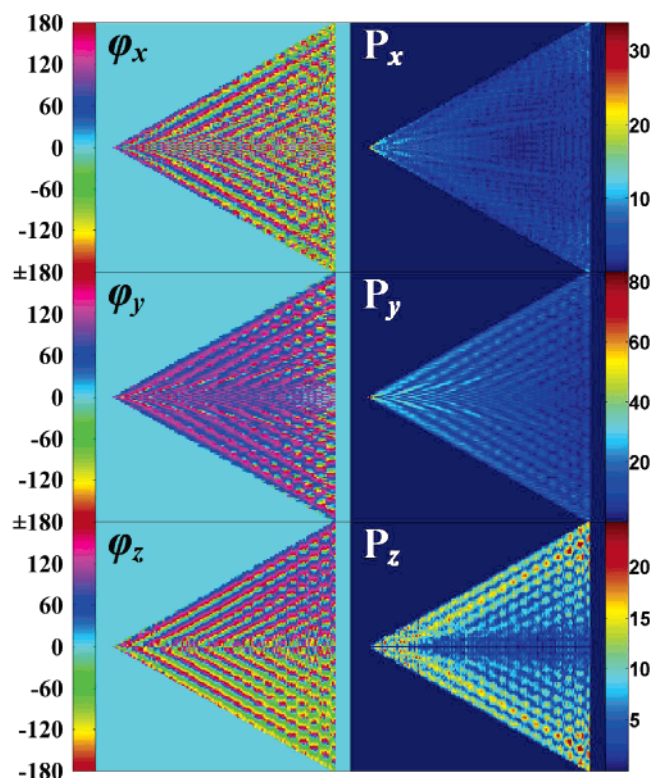


**Figure 4.** Six-parameter plots of the dipoles in the  $x = 0$  plane; the triangle nanoplate 150-10 is irradiated by an incidence with the wavelength of 805 nm (Mode-I).

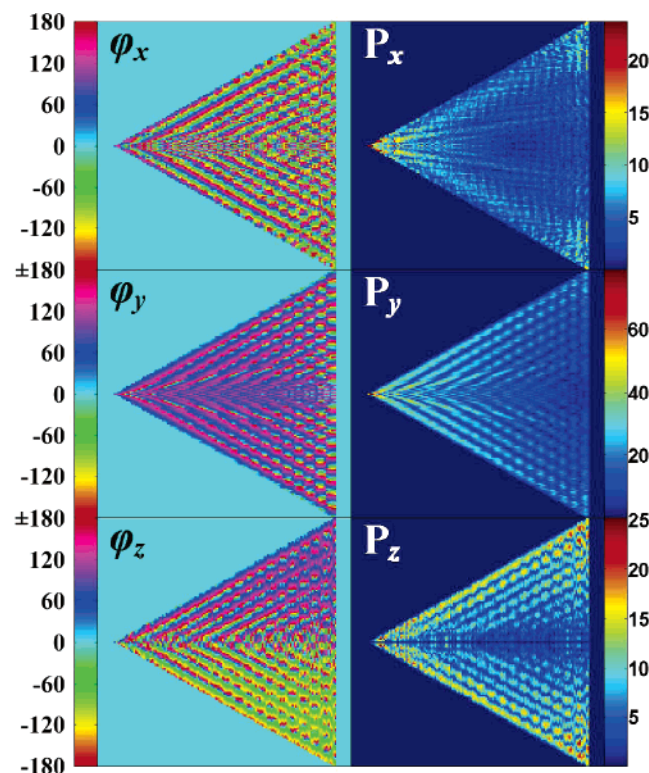


**Figure 5.** Six-parameter plots of the dipoles in the  $x = 1$  plane; the triangle nanoplate 150-10 is irradiated by an incidence with the wavelength of 805 nm.

change the position of a nanoplate along the  $x$ -axis (just translation, no rotation) in the geometric setups, the phase values of all the dipoles of this nanoplate will change. However, the phase angle difference between any two dipoles, for example,  $\varphi_{i,x} - \varphi_{j,x}$ , is independent of the position of the nanoplate. Since two adjacent basic oscillations with four typical phase differences can give four distinguishing physical views as illustrated in Table 1, a large number of dipoles with arbitrary phase differences will cause so complex a situation that a colorful graph is entailed to image it. The three plots on the right of Figure 4 correspond to the distributions of three amplitudes  $P_x$ ,  $P_y$ , and  $P_z$ , which are no less important than those of the phase angles. Three color bars are attached to the right of the plots respectively and the values of amplitudes can be roughly estimated from them. As a result, the combination of the six plots provides a possibility to embody the SPR mode and inform us of some useful details of the global oscillation of conductive electrons.

The dipoles in the plane  $x = 1$ , which is neighboring the plane  $x = 0$ , is illustrated in Figure 5 by the same method. The dipoles in the rest of the eight planes  $x = 2, \dots, 9$  are imaged in the Supporting Information (Figure S1–S8). These pictures display almost the same pattern except for some fine features of amplitudes. After careful consideration we select the plane  $x = 0$  as the key plane for characterizing the SPR mode, because it has the strongest amplitudes in the distributions of  $P_x$  and  $P_y$ , and comparative intensity in  $P_z$ . For the same reason, the other two SPR modes of 150-10 will be characterized by imaging the dipoles in the plane  $x = 0$ , as well as all the SPR modes of the other four nanoplates.

Something about symmetries should be mentioned here. In the distributions of  $\varphi_x$ ,  $\varphi_y$ ,  $P_x$ ,  $P_y$ , and  $P_z$ , the upper half of each triangle is symmetrical to its lower half, as shown in Figures 4 and 5. In other words, these five parameters are

symmetrical about the plane  $z = 0$ . However, the  $\varphi_z$  of all the dipoles in the upper half of the triangle has a phase difference of  $180^\circ$  with the  $\varphi_z$  of the corresponding dipole in the lower half. This indicates the  $z$ -components of two dipoles always have contrary signs due to the property of cosine function. Thus,  $\varphi_z$  is antisymmetrical about the plane  $z = 0$ . Generally, the symmetry of the SPR mode is a function of the target shapes, propagation directions, and polarization states of the incidences, while it is independent of the wavelength of incidence. In this paper, the calculations are based on the same target shape (triangle plate), fixed propagation direction, and polarization state. So all the results presented in this paper will share the same symmetries as Figure 4.

**3.3. Graphical Assignments of the SPR Modes.** A conspicuous feature of Figure 4 is the stripes extending through the whole triangle cross section, especially in the distributions of  $\varphi_y$ ,  $\varphi_z$ ,  $P_y$ , and  $P_z$ . After a cautious comparison between the plots of  $\varphi_y$  and  $P_y$ , we find the light blue stripes (indicating strong amplitudes of ca. 30) in the  $P_y$  distribution always correspond to the blue stripes (indicating phase angles of ca.  $60^\circ$ ) in the  $\varphi_y$  distribution. This means that the two patterns are coincident to each other exactly. The same character also exists among the upper half of  $\varphi_z$  and  $P_z$ . If we ignore the antisymmetry of the lower half of  $\varphi_z$ , it also corresponds to the lower half of the  $P_z$ . Furthermore,  $\varphi_y$  and  $\varphi_z$  have similar stripes. They have almost the same phases in their upper half parts and almost opposite phases (with a difference of  $180^\circ$ ) in their lower half parts. So the resultant of the  $y$ - and  $z$ -components generates two sets of parallel oscillatory stripes in the  $yOz$  plane. The upper stripes are parallel to the upper side of the triangle, while the lower stripes are parallel to the lower side. The images of  $\varphi_x$  and  $P_x$  in Figure 4 are not similar to those of the others. In spite of there being some stripes in the distribution of  $\varphi_x$ , the distribution of  $P_x$  is irregular and it gives little information. In brief, the most intensive amplitudes appear at the vertexes of the triangle, then extend and decrease along the two sides, and the weakest amplitudes appear at the center of the triangle.

The SPR Mode-I of nanoplates 250-10, 200-10, 100-10, and 50-10 at corresponding wavelengths are illustrated in Figures 6 to 9, respectively. Despite the obvious difference in their side lengths, these four nanoplates all present features similar to those of nanoplate 150-10 shown in Figure 4. Therefore, the conclusions derived from Figure 4 can be extended to the analyses and characterizations of the SPR Mode-I of the other four nanoplates. The result indicates classifying the dominant peak of each spectrum into the same mode is fairly reasonable. The graphic assignments of SPR Mode-I of triangle nanoplates are based on the features of these figures and the related analyses of the  $x$ -,  $y$ -, and  $z$ -components.

As an empirical rule, a SPR mode can be classified according to its wavelength value. However, following the graphic assignments, we found that the SPR peak of the nanoplate 250-10 at 1052 nm and that of 50-10 at 541 nm belong to the same SPR mode and the value of the former peak is nearly twice that of the later. Should the SPR peaks at close positions be assigned to same mode? Now we come back to the inset of Figure 3, in which there are three peaks in the range of 520 to 570 nm. They are SPR Mode-III of 250-10 at 529 nm, SPR Mode-I of 50-10 at 541 nm, and SPR Mode-II of 200-10 at 552 nm, respectively, with intervals of only 12 or 11 nm. The SPR Mode-I of 50-10 at 541 nm has been graphically illustrated in Figure 9, and the other two are pictured in Figures 10 and 11, which evidently differ from those of Mode-I. Furthermore,



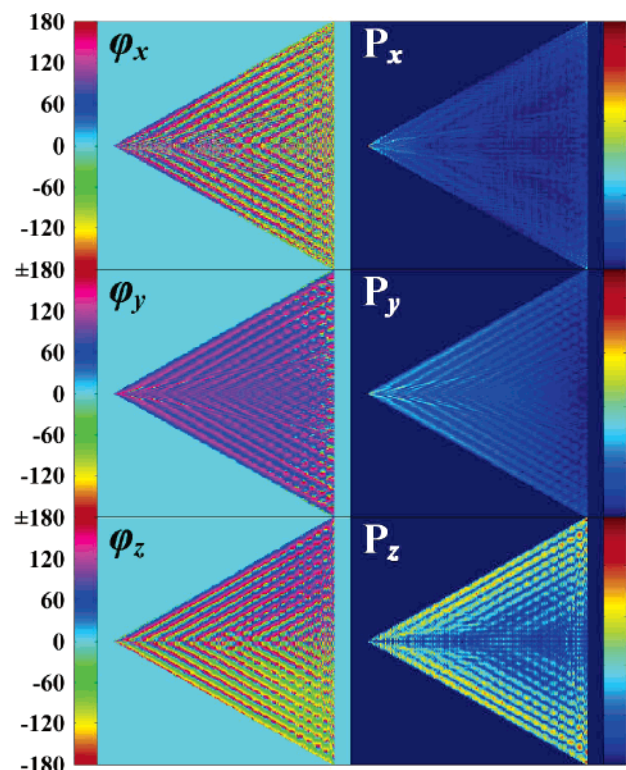


**Figure 6.** Six-parameter plots of the dipoles in the  $x = 0$  plane; the triangle nanoplate 250-10 is irradiated by an incidence with the wavelength of 1052 nm (Mode-I).

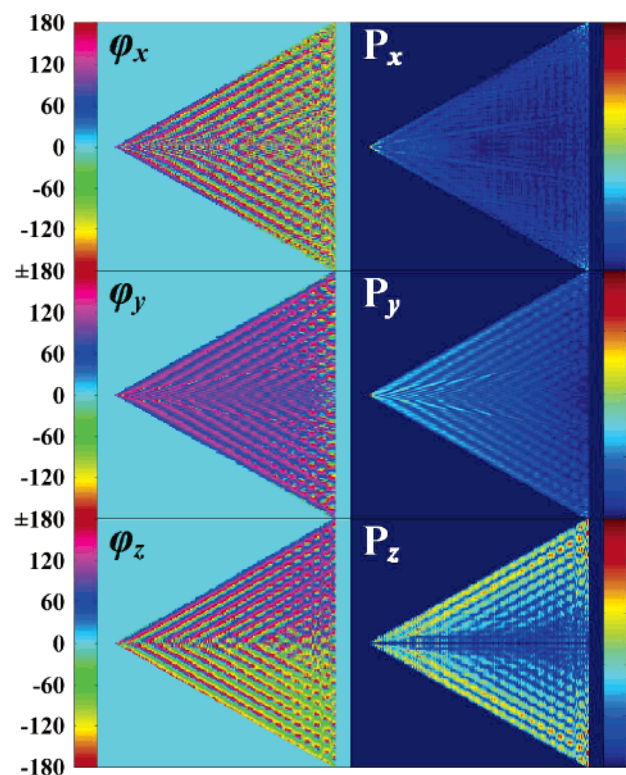


**Figure 7.** Six-parameter plots of the dipoles in the  $x = 0$  plane; the triangle nanoplate 200-10 is irradiated by an incidence with the wavelength of 924 nm (Mode-I).

the two new modes are different from each other. We can easily differentiate them according to their fine features. For example, there are several domains with intensive amplitudes in the upper half of the triangle of  $P_z$  distribution in Figure 11, whereas in Figure 10 these domains almost merge into one. In addition,

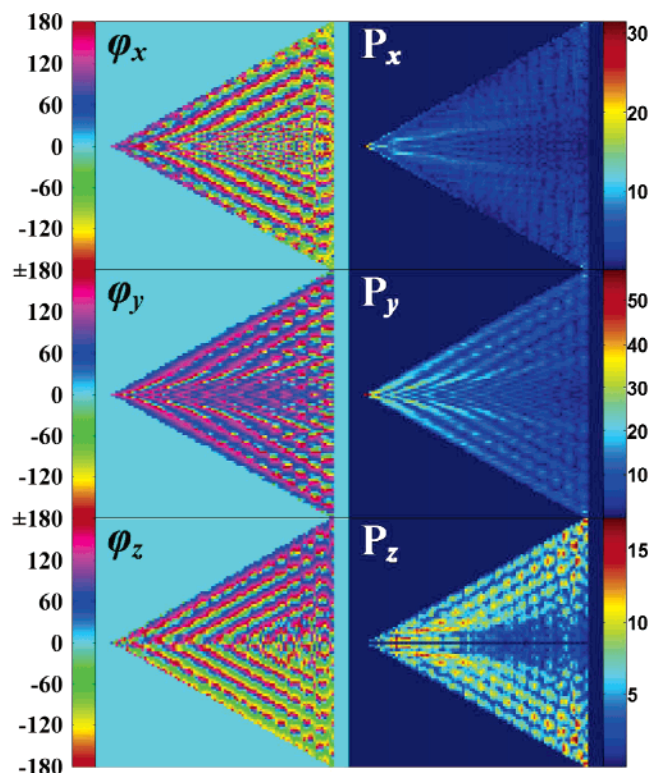


**Figure 8.** Six-parameter plots of the dipoles in the  $x = 0$  plane; the triangle nanoplate 100-10 is irradiated by an incidence with the wavelength of 680 nm (Mode-I).

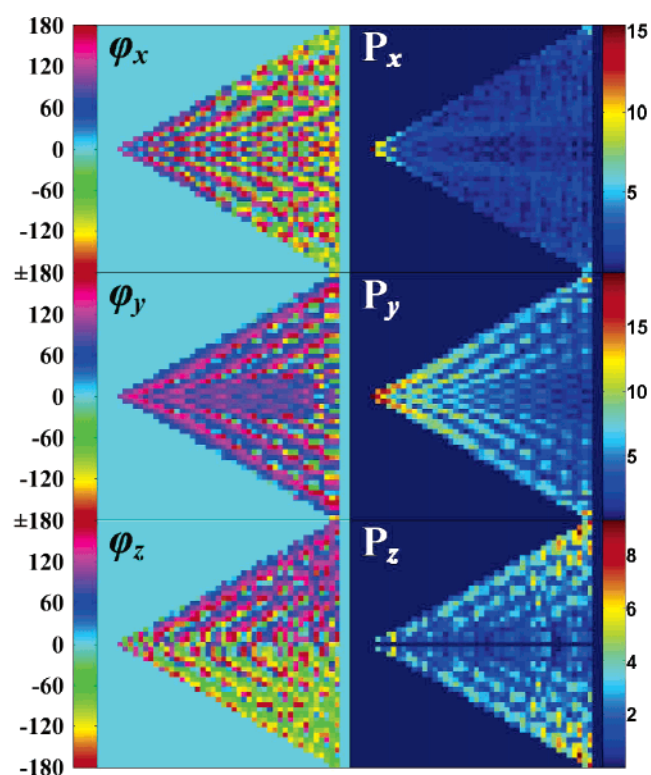


**Figure 9.** Six-parameter plots of the dipoles in the  $x = 0$  plane; the triangle nanoplate 50-10 is irradiated by an incidence with the wavelength of 541 nm (Mode-I).

there are many detailed differences between the patterns of corresponding phase angles, which act as fingerprints for the recognition. Therefore, the three SPR modes are different in nature and we cannot take them as one just due to their close wavelengths. The SPR Mode-II of 50, 100, 150, 250-10 and

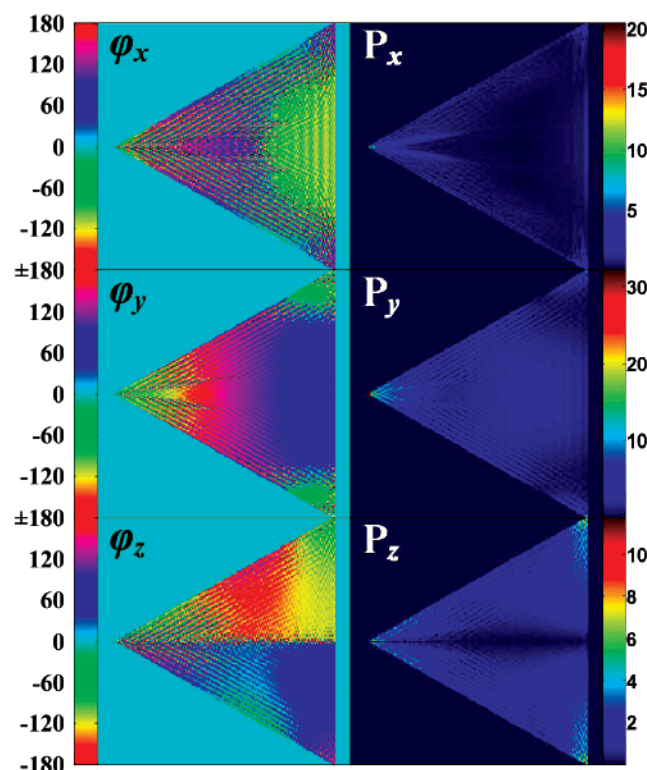


**Figure 10.** Six-parameter plots of the dipoles in the  $x = 0$  plane; the triangle nanoplate 200-10 is irradiated by an incidence with the wavelength of 552 nm (Mode-II).

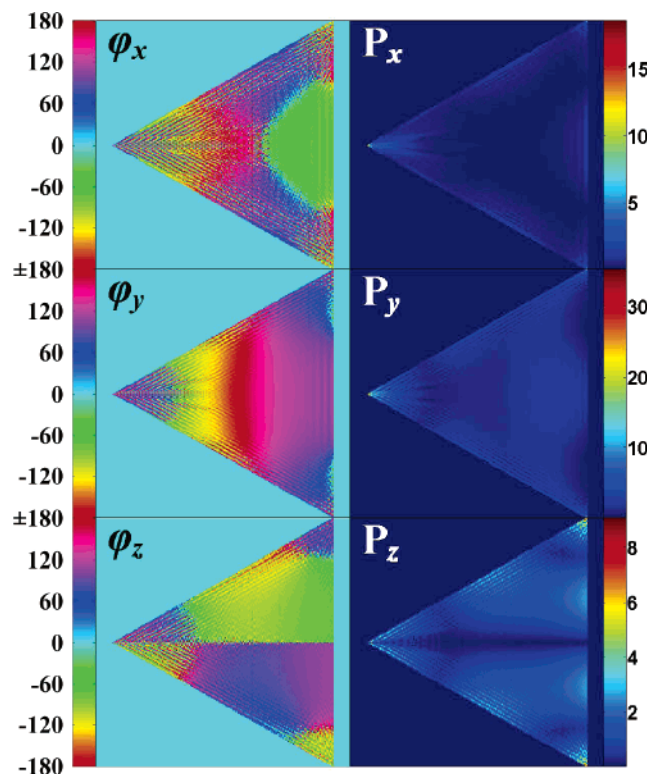


**Figure 11.** Six-parameter plots of the dipoles in the  $x = 0$  plane; the triangle nanoplate 250-10 is irradiated by an incidence with the wavelength of 529 nm (Mode-III).

SPR Mode-III of 50, 100, 150, 200-10 are presented in Figures S9–S16 (Supporting Information), respectively, as supplementary evidence. The figures of the same mode always possess identical characteristics, so a classification based on the graphic analysis described above is more credible.

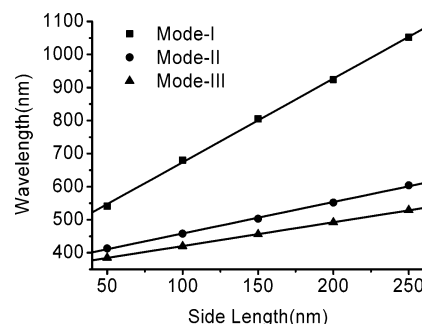


**Figure 12.** Linear fittings of the SPR peaks of three SPR modes vs the side lengths of the triangle nanoplates.

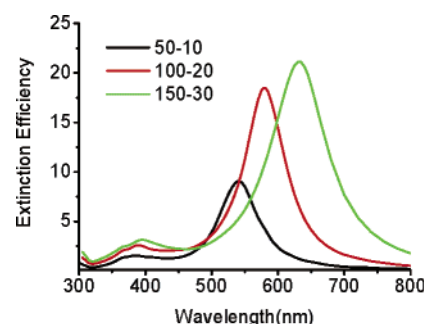


**Figure 13.** The calculated extinction spectra of the three triangle nanoplates 50-10, 100-20, and 150-30.

**3.4. Linear Fittings of the SPR Peaks.** Since the SPR peaks of a certain mode are correlated with each other, we will establish a numerical relation between the wavelength of the SPR peak and the side length of the silver nanoplate for each SPR mode. Figure 12 demonstrates that each SPR mode presents a good linear character, and the linear equations of the three modes are  $y = 2.532x + 420.6$  (Mode-I),  $y = 0.952x + 363.2$  (Mode-II), and  $y = 0.720x + 348.4$  (Mode-III), respectively. Here  $y$  and  $x$  denote the wavelength of the peak and the side length of the nanoplate, respectively. The result indicates that the wavelengths of the SPR peaks of a triangle nanoplate with a thickness of 10 nm and an arbitrary side length can be easily estimated without performing any DDA calculations, which may be a time-consuming job. On the other hand, giving a main SPR wavelength, a corresponding side length is determined according to  $x = (y - 420.6)/2.532$ . So it can provide a direction in the syntheses of silver nanoplates with SPR peaks of desired wavelengths, and this point is very helpful for design and application of the nanomaterials.

There are two things that should be mentioned here. First, with the decrease of the side length, the geometric character of the target as a triangle plate disappears and it become more like a sphere. So the side length of the triangle should not be too small (longer than 40 nm), or the result will diverge from the fittings quite a bit. For example, the SPR Mode-I of the triangle 30-10 is at a wavelength of 477 nm, far from the estimated value of 497 nm. Second, the side length is used as the abscissa in Figure 12, instead of the ratio between the side length and the thickness ( $a/h$ ) of a nanoplate. Here we perform the spectrum simulations of another two triangle nanoplates, one with a thickness of 20 nm and a side length of 100 nm, the other with a thickness of 30 nm and a side length of 150 nm. They are denoted by 100-20 and 150-30, respectively, and their extinction spectra with that of 50-10 are shown in Figure 13. Despite the same ratio of  $a/h$ , their curves display notable differences, especially the traces of the SPR Mode-I, which cannot be attributed to the error of the simulations. It implies



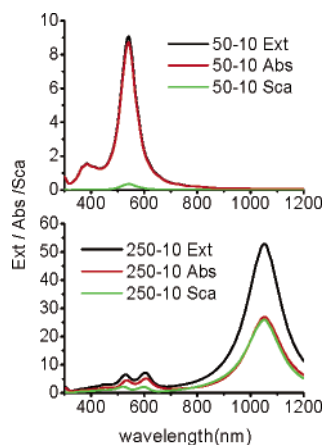


**Figure 14.** The calculated extinction (Ext), absorption (Abs), and scattering (Sca) spectra of the two triangle nanoplates 50-10 and 250-10.

**TABLE 4. The Relative Contributions of Absorption to the SPR Modes of the Five Triangle Nanoplates**

	50-10	100-10	150-10	200-10	250-10
Mode-I	0.961	0.848	0.691	0.582	0.509
Mode-II	0.987	0.950	0.888	0.801	0.711
Mode-III	0.983	0.928	0.843	0.753	0.677

that the thickness influences the SPR of the triangle nanoplate as well as the side length, so the two factors should not be simplified to a ratio. However, it is possible to carry out analogous calculations with different thicknesses and set up a universal formula that contains both the side length and the thickness of the triangle plates.

**3.5. Scattering and Absorption.** As has been expressed in eq 8, the extinction efficiency of the silver nanoparticles is the sum of two parts, absorption and scattering. The former component transforms the radiation energy into heat while the latter scatters the incidence into the full solid angle. Theoretical and experimental results have demonstrated that the relative contribution of these two components to each SPR mode of nanospheres is determined by particle radius.<sup>10</sup> However, there is little investigation about the particles with other shapes, even the triangle plate. Absorption and scattering spectra of two triangle nanoplates 50-10 and 250-10 as well as their extinction spectra are shown in Figure 14. As can be seen from this figure, absorption is the predominant component of the three modes of 50-10. The contribution of the scattering effect grows with the increase of side length. Typically, the relative contribution of the absorption for Mode-I of 50-10 is 0.961, while this value drops to 0.509 for Mode-I of 250-10. As listed in Table 4, a longer side length leads to a more intensive scattering and it reduces the relative contribution of absorption. This rule is more evident to Mode-I, the dominant SPR peak in a spectrum. The trend conforms substantially to the experiments reported by Chumanov,<sup>10b</sup> though their experiments concerned the quasi-sphere in water while our simulations are about triangle plates in a vacuum.

#### 4. Conclusion

The DDA method was utilized to simulate the extinction spectra of five silver triangle nanoplates with fixed thickness of 10 nm and various side lengths of 50, 100, 150, 200, and 250 nm. The graphic analysis method has been proven to be useful in characterizations and assignments of the SPR peaks, because it can provide direct graphic evidence for deciding the

SPR modes. In this way, three distinct SPR modes are recognized and their linear dependence on the side length of the triangle is revealed by fitting the data. At last, the absorption and scattering of the nanoplates with a given thickness depend strongly on their side lengths, and the relative contribution of scattering increases with the increase of side length of the nanoplate.

**Acknowledgment.** We thank the support of National Natural Science Foundation of China with grant Nos. 90401011, 20374034, and 50225311 and the 973 Project with grant No. 2003CB615700.

**Supporting Information Available:** Supplemental figures regarding the six-parameter plots of the eight planes ( $x = 2, \dots, 9$ ) of 150-10 at 805 nm, as well as the SPR Mode-II and Mode-III of different triangle nanoplates. This material is available free of charge via the Internet at <http://pubs.acs.org>.

#### References and Notes

- (1) (a) Templeton, A. C.; Wuelfing, W. P.; Murray, R. W. *Acc. Chem. Res.* **2000**, *33*, 27. (b) El-Sayed, M. A. *Acc. Chem. Res.* **2001**, *34*, 257. (c) Mulvaney, P. *Langmuir* **1996**, *12*, 788.
- (2) (a) Martin, J. E.; Wilcoxon, J. P.; Odinek, J.; Provencio, P. *J. Phys. Chem. B* **2000**, *104*, 9475. (b) He, S. T.; Yao, J. N.; Jiang, P.; Shi, D. X.; Zhang, H. X.; Xie, S. S.; Pang, S. J.; Gao, H. J. *Langmuir* **2001**, *17*, 1571. (c) Stoeva, S. I.; Prasad, B. L. V.; Uma, S.; Stoimenov, P. K.; Zaikovski, V.; Sorensen, C. M.; Klabunde, K. J. *J. Phys. Chem. B* **2003**, *107*, 7441.
- (3) (a) Sun, Y. G.; Xia, Y. N. *Science* **2000**, *298*, 2176. (b) Yu, D. B.; Yam, V. W. W. *J. Am. Chem. Soc.* **2004**, *126*, 13200.
- (4) (a) Chen, S. H.; Wang, Z. L.; Ballato, J.; Foulger, S. H.; Carroll, D. L. *J. Am. Chem. Soc.* **2003**, *125*, 16186. (b) Hao E. C.; Bailey, R. C.; Schatz, G. C.; Hupp J. T.; Li, S. Y. *Nano Lett.* **2004**, *4*, 327.
- (5) (a) Cepak V. M.; Martin C. R. *J. Phys. Chem. B* **1998**, *102*, 9985. (b) Nikoobakht, B.; El-Sayed, M. A. *Chem. Mater.* **2003**, *15*, 1957. (c) Hu, J. Q.; Chen, Q.; Xie, Z. X.; Han, G. B.; Wang, R. H.; Ren, B.; Zhang, Y.; Yang, Z. L.; Tian, Z. Q. *Adv. Func. Mater.* **2004**, *14*, 183.
- (6) (a) Jana, N. R.; Gearheart, L.; Murphy, C. J. *Chem. Commun.* **2001**, 617. (b) Tao, A.; Kim, F.; Hess, C.; Goldberger, J.; He, R. R.; Sun, Y. G.; Xia Y. N.; Yang, P. D. *Nano Lett.* **2003**, *3*, 1229.
- (7) (a) Hao, E. C.; Kelly, K. L.; Hupp, J. T.; Schatz, G. C. *J. Am. Chem. Soc.* **2002**, *124*, 15182. (b) Maillard, M.; Giorgio, S.; Pileni, M. P. *Adv. Mater.* **2002**, *14*, 1084. (c) Sun, X. P.; Dong, S. J.; Wang, E. K. *Angew. Chem., Int. Ed.* **2004**, *43*, 6360. (d) Kim, J. U.; Cha, S. H.; Shin, K. S.; Jho, J. Y.; Lee, J. C. *Adv. Mater.* **2004**, *16*, 459. (e) He, Y.; Wu, X. F.; Lu, G. W.; Shi, G. Q. *Nanotechnology* **2005**, *16*, 791.
- (8) (a) Jin, R. C.; Cao, Y. W.; Mirkin C. A.; Kelly, K. L.; Schatz, G. C.; Zheng, J. G. *Science* **2001**, *294*, 1901. (b) Sun, Y. G.; Xia, Y. N. *Adv. Mater.* **2003**, *15*, 695. (c) Jiang, L. P.; Xu, S.; Zhu, J. M.; Zhang, J. R.; Zhu, J. J.; Chen, H. Y. *Inorg. Chem.* **2004**, *43*, 5877.
- (9) (a) Mock, J. J.; Barbic, M.; Smith, D. R.; Schultz, D. A.; Schultz, S. J. *Chem. Phys.* **2002**, *116*, 6755. (b) Yacamán, M. J.; Ascencio, J. A.; Liu, H. B.; Gardea-Torresdey, J. J. *Vac. Sci. Technol. B* **2001**, *19*, 1091. (c) Kottmann, J. P.; Martin, O. J. F.; Smith, D. R.; Schultz, S. *Phys. Rev. B* **2001**, *64*, 235402.
- (10) (a) Messinger, B. J.; von Raben, K. U.; Chang, R. K.; Barber, P. W. *Phys. Rev. B* **1981**, *24*, 649. (b) Evanoff, D. D.; Chumanov, G. *J. Phys. Chem. B* **2004**, *108*, 13957.
- (11) Jin, R. C.; Cao, Y. C.; Hao, E. C.; Metraux, G. S.; Schatz, G. C.; Mirkin, C. A. *Nature* **2003**, *425*, 487.
- (12) (a) Alivisatos, P. *Nat. Biotechnol.* **2003**, *100*, 13549. (b) Sershen, S. R.; Westcott, S. L.; Halas, N. J.; West, J. L. *J. Biomed. Mater. Res.* **2000**, *51*, 293. (c) West, J. L.; Halas, N. J. *Annu. Rev. Biomed. Eng.* **2003**, *5*, 285.
- (13) Faraday, M. *Philos. Trans.* **1857**, *147*, 145.
- (14) Mie, G. *Ann. Phys.* **1908**, *25*, 377.
- (15) (a) Purcel, E. M.; Pennypacker, C. R. *Astrophys. J.* **1973**, *186*, 705. (b) Draine, B. T.; Flatau, P. J. *J. Opt. Soc. Am. A* **1994**, *11*, 1491. (c) Shang, J. S. *J. Comput. Phys.* **1996**, *128*, 381. (d) Waterman, P. C. *Phys. Rev. D* **1971**, *3*, 825. (e) Moreno, E.; Erni, D.; Hafner, C.; Vahldieck, R. *J. Opt. Soc. A* **2002**, *19*, 101.
- (16) Yang, W. H.; Schatz, G. C.; Van Duyne, R. P. *J. Chem. Phys.* **1995**, *103*, 869.
- (17) (a) Malinsky, M. D.; Kelly, K. L.; Schatz, G. C.; Van Duyne, R. P. *J. Phys. Chem. B* **2001**, *105*, 2343. (b) Salzemann, C.; Lisiecki, I.; Brioude, A.; Urban, J.; Pileni, M. P. *J. Phys. Chem. B* **2004**, *108*, 13242. (c) Su, K. H.; Wei, Q. H.; Zhang, X.; Mock, J. J.; Smith, D. R.; Schultz,



- S. *Nano Lett.* **2003**, 3, 1087. (d) Yang, Z. L.; Hu, J. Q.; Li, X. Y.; Zhou, H. G.; Tian, Z. Q. *Chin. J. Chem. Phys.* **2004**, 17, 253.
- (18) (a) Sosa, I. O.; Noguez, C.; Barrera, R. G. *J. Phys. Chem. B* **2003**, 107, 6269. (b) Felidj, N.; Aubard, J.; Levi, G. *J. Chem. Phys.* **1999**, 111, 1195.
- (19) Kreibig, U.; Schmitz, B.; Breuer, H. D. *Phys. Rev. B* **1987**, 36, 5027.
- (20) Kelly, K. L.; Coronado, E.; Zhao, L. L.; Schatz, G. C. *J. Phys. Chem. B* **2003**, 107, 668.
- (21) Draine, B. T.; Goodman, J. *Astrophys. J.* **1993**, 405, 685.

- (22) Lynch, D. W.; Hunter, W. R. In *Handbook of Optical Constants of Solids*; Palik, E. D., Ed.; Academic Press: New York, 1985; pp 350–356.
- (23) (a) Draine, B. T.; Flatau, P. J. *Program DDSCAT*, version 6.0; University of California: San Diego, CA; Scripps Institute of Oceanography: La Jolla, CA, 2003. (b) Draine, B. T. *Astrophys. J.* **1988**, 333, 848. (c) Goodman, J. J.; Draine, B. T.; Flatau, P. J. *Opt. Lett.* **1991**, 16, 1198.
- (24) Bohren, C. F.; Huffman, D. R. *Absorption and Scattering of Light by Small Particles*; Wiley-Interscience: New York, 1983.